Heavy fermions, metal-to-insulator transition, and quantum criticality in $\mathrm{La}_y\mathrm{Cu}_3\mathrm{Ru}_x\mathrm{Ti}_{4-x}\mathrm{O}_{12}$

S. Riegg[1], S. Widmann[1], A. Günther[1], B. Meir[1], S. Wehrmeister[1], S. Sterz[1],
W. Kraetschmer[1], S.G. Ebbinghaus[2], A. Reller[3], N. Büttgen[1],
H.-A. Krug von Nidda[1], and A. Loidl[1,a]

[1] Experimental Physics V, Center for Electronic Correlations and Magnetism,
    University of Augsburg, 86159 Augsburg, Germany
[2] Solid State Chemistry, Martin-Luther-University Halle-Wittenberg, 06099 Halle,
    Germany
[3] Resource Strategy, University of Augsburg, 86159 Augsburg, Germany

Abstract. In this work we investigate the solid-solution series $\mathrm{La}_y\mathrm{Cu}_3\mathrm{Ru}_x\mathrm{Ti}_{4-x}\mathrm{O}_{12}$. The titanate $\mathrm{La}_{2/3}\mathrm{Cu}_3\mathrm{Ti}_4\mathrm{O}_{12}$ ($x=0$) is an antiferromagnetic insulator exhibiting colossal dielectric constants, while the ruthenate $\mathrm{LaCu}_3\mathrm{Ru}_4\mathrm{O}_{12}$ ($x=4$) is known as a rare d-electron derived heavy-fermion compound. Detailed structural investigations, AC- and DC-magnetization measurements, resistivity, specific-heat, and magnetic-resonance investigations have been performed for all polycrystalline compounds prepared by solid-state synthesis. These experiments have been accompanied by band-structure calculations. Close to the Ru concentration $x = 2$ we identify a quantum-critical point coinciding with a metal-to-insulator transition. The quantum-critical point separates an insulating spin glass from a paramagnetic metal. Interestingly, there is no evidence for a divergence of the effective mass upon reaching the quantum-critical point from the metallic side. In the paramagnetic metal, Ru behaves like a canonical Kondo ion. While the Ru oxidation state remains stable at $+4$ for the whole concentration regime, the Cu valence seems to decrease from $+2$ in the insulating antiferromagnet with localized copper spins to a significantly lower value in the metallic heavy-fermion compounds.

1 Introduction

Transition-metal compounds of the perovskite-related superstructure $AA'_3B_4\mathrm{O}_{12}$ are derived from the parent compounds $AB\mathrm{O}_3$ by substituting three fourths of the A-site cations by Jahn-Teller active atoms like Cu^{2+} or Mn^{3+}. A collective rotation of the $B\mathrm{O}_6$-octahedra leads to a new crystallographic A'-site with square-planar coordination and yields doubling of the perovskite unit cell along all three directions,

leaving the overall cubic symmetry intact. The $AA'_3B_4O_{12}$ compounds show a variety of different electronic and magnetic ground states. $CaCu_3Ti_4O_{12}$, for instance, gained considerable interest due to the occurrence of colossal dielectric constants [1,2]. $CaCu_3Mn_4O_{12}$ is an insulating ferromagnet with an ordering temperature of 360 K [3] and $CaCu_3Ru_4O_{12}$ is a heavy-fermion metal with strongly enhanced effective masses of the band-state electrons [4–6]. The formation of heavy fermions in transition-metal oxides is still a matter of debate and of current interest. Conventional f-electron based heavy fermions are formed by hybridization between localized f electrons of rare-earth or actinide compounds and mainly s- and p-derived conduction electrons. However, heavy-fermion behavior has also been detected in LiV_2O_4 where strong electronic correlations result from hybridization of partly localized with delocalized d-electrons of the vanadium ions [7,8]. In addition, clear evidence for non-Fermi liquid behavior has been detected in $CaCu_3Ru_4O_{12}$ below 2 K and this compound has been identified as being the first intermediate-valence system among transition-metal compounds [9].

To further elucidate the electronic correlations in $CaCu_3Ru_4O_{12}$, it seems interesting to follow the evolution of heavy fermion to insulating and antiferromagnetic behavior by substituting titanium for ruthenium. The synthesis of this solid solutions has been reported earlier [4,10,11]. However, it is our believe that in the Ca compounds a miscibility gap shows up at intermediate concentrations and that the full concentration regime between titanium and ruthenium is not accessible. It has been shown that in the $ACu_3Ru_4O_{12}$ compounds, the A-site can also be occupied by different rare-earth ions, namely by La, Pr, and Nd [10,12–16]. Smaller trivalent rare-earth ions such as Sm^{3+} seem to destabilize the perovskite derived structure due to the smaller size compared to Ca^{2+}. On the other hand, for $A = Sr^{2+}$, which is larger than La^{3+}, only the pure titanate and ruthenate are available [13,17].

In this work we document that the whole solid solution can be obtained for the La compounds [15]. The samples were prepared using solid-state synthesis and were characterized by x-ray diffraction. The magnetic properties were investigated using susceptibility and magnetic-resonance techniques. In addition, we present detailed resistivity and heat-capacity results as function of temperature. The evolution of the ground state from the heavy-fermion behavior in $LaCu_3Ru_4O_{12}$ to insulating antiferromagnetic $La_{2/3}Cu_3Ti_4O_{12}$ is followed in detail. We report the occurrence of a metal-to-insulator transition coinciding with a quantum-critical point where magnetic order finally becomes suppressed. In addition, we show how the stable divalent Cu ions with spin $S = 1/2$ in the antiferromagnetic insulator becomes destabilized, taking over the role of band states and hybridizing with the ruthenium moments. Hence, on the metallic side, but still at low ruthenium concentrations the system reveals Kondo-like physics, which results in strong electronic correlations with concomitant heavy masses when reaching the full ruthenium concentration $x = 4$. These investigations in $La_yCu_3Ru_xTi_{4-x}O_{12}$ show how quantum criticality, Kondo physics, metal-to-insulator transition and heavy-fermion behavior can be studied in one solid-solution system without additional rare-earth derived $4f$ moments at all.

2 Synthesis and experimental details

2.1 Synthesis

Polycrystalline samples of $La_yCu_3Ru_xTi_{4-x}O_{12}$ were prepared from a mixture of La_2O_3, TiO_2, RuO_2, and CuO in corresponding molar ratios to obtain 2 g of the final product [10,12,15,18,19]. An excess of CuO (roughly 0.3 g per g of final product) was added as self-flux. This CuO excess was removed after the calcination using diluted

hydrochloric acid. The ground starting mixture was pelletized to avoid reaction with the crucible material. The pellets were heated in air between $1000°C$ and $1040°C$ for at least 96 hours with intermediate grindings after 48 hours. The phase purity was checked by x-ray powder diffraction after each calcination step. The required calcination temperature depends on the composition. Pure titanate samples ($x = 0$) were reacted at $1000°C$, while Ru containing samples were heated to $1040°C$ to achieve single-phase material. The titanate powders exhibit an orange-brownish color, however, only a minor substitution of Ru ($x > 0$) for Ti turns the color of the powders to black.

Due to the $+3$ valence of the rare-earth metal ion the samples with $x < 0.33$ possess an A-site deficiency. In the pure titanates $1/3$ of the A-sites remain unoccupied with sum formula $Ln_{2/3}Cu_3Ti_4O_{12}$ (Ln = lanthanide element) [20]. The increasing Ru content x is accompanied by a concomitantly increasing A-site occupation y according to $y = 2/3 + x$ (for $x \leq 1/3$). Thus, starting with the compounds $LaCu_3Ru_{0.33}Ti_{3.67}O_{12}$ ($x = 0.33$) the fully occupied A-site is reached for all samples until $x = 4$. To indicate these complex rules the samples are denoted $La_yCu_3Ru_xTi_{4-x}O_{12}$, where y marks the (deficient) A-site occupancy.

For ESR investigations Gd^{3+} ions were additionally substituted on the A-site for $1 \leq x \leq 4$. For the synthesis the corresponding molar amount of Gd_2O_3 was used instead of La_2O_3, applying the same temperature steps and preparation conditions as for $La_yCu_3Ru_xTi_{4-x}O_{12}$ leading to samples with chemical composition $La_{0.95}Gd_{0.05}Cu_3Ru_xTi_{4-x}O_{12}$ [21].

2.2 Experimental details

Room temperature x-ray diffraction patterns were recorded using a *Seifert TT3003* diffractometer equipped with a *METEOR 1D* detector. Cu-K$_{\alpha 1,2}$ radiation was used to measure the patterns in the angular range $15° \leq 2\theta \leq 100°$ with a step width of $0.01°$. The patterns were analyzed by Rietveld-refinement utilizing the *FullProf*-program suite [22].

Magnetic susceptibilities in the temperature range $2\,K \leq T \leq 400\,K$ were measured using a SQUID magnetometer *MPMS-XL* (*Quantum Design*). For the DC-susceptibility measurements an external field of 1000 Oe was used. Measurements under field cooled (FC) and zero-field cooled (ZFC) conditions were performed at $H = 100$ Oe or 1000 Oe. AC-susceptibility measurements were carried out with an AC-magnetic field $H_{AC} = 2$ Oe applying frequencies between $0.4\,Hz$ and $1113\,Hz$.

The specific heat was measured in the temperature range $1.8\,K \leq T \leq 300\,K$ using a physical properties measurement system PPMS (*Quantum Design*). For the resistivity measurements, the polycrystalline samples were pressed to square bars of $13 \times 2 \times 2\,mm^3$, sintered for 10 hours at $1000\,°C$ and contacted with silver paint. The measurements were performed with four point method in the *Quantum Design* PPMS in a temperature range between $1.8\,K$ and $300\,K$.

For ESR experiments we used a *Bruker ELEXSYS E500* spectrometer working at X-band frequency ($9.4\,GHz$) while for NQR we employed a home built setup. The homodyne demodulation of the radio-frequency (RF) nuclear signals was achieved by digital quadrature detection using a fast two-channel oscilloscope card.

Electronic band-structure calculations were performed using the full-potential local-orbital minimum base code *FPLO* 7.00-28 [23,24]. The crystal-structure data obtained from XRD Rietveld refinement were used as input data. The symmetry was lowered to $P1$ (SG no. 1) to replace single Ru ions by Ti and to study the magnetic interaction of the Ru ions by using local spin-density approximation (LSDA). The number of k points in the reciprocal lattice was adapted to the reciprocal unit-cell
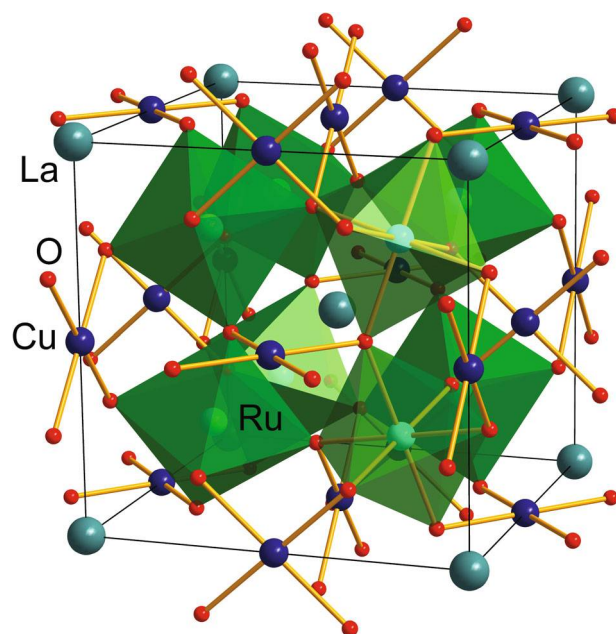
Fig. 1. Crystal structure of $AA'_3B_4O_{12}$. The structure is closely related to $2\times2\times2$ perovskite unit cells with rotated BO_6 octahedra caused by the insertion of Jahn-Teller active ions on $3/4$ of the A-site, which is leading to the additional A'-sites. The A-site ions (La) are represented by large turquoise spheres, the oxygen ions are drawn as small red spheres, and the BO_6 octahedra (Ru,Ti) are colored green. The A'-site ions (Cu) are colored dark blue and the square-planar coordination is highlighted by yellow A'–O bonds.

axis lengths and set to $4 \times 4 \times 4$ according to literature. A scalar-relativistic setting was used for the calculations.

3 Structural properties

$La_yCu_3Ru_xTi_{4-x}O_{12}$ is based on a $2 \times 2 \times 2$ superstructure of the perovskite ABO_3 unit cell. The specific crystal structure results from a cooperative rotation of the BO_6 octahedra around $\langle111\rangle$ corresponding to a threefold tilting according to $a^+a^+a^+$ in the Glazer notation [25,26]. This leads to a general sum formula $AA'_3B_4O_{12}$ for these oxides, which crystallize in the space group $Im\bar{3}$ (No. 204). The A-cation occupies the Wyckoff-site $2a$ with relative coordinates 0 0 0. Three quarters of the former perovskite A-site[1] possess a strongly deformed cuboctahedral, almost square-planar, coordination, expressed by the changed notation A'. Due to this coordination the A'-sites ($6b$: 0 $\frac{1}{2}$ $\frac{1}{2}$) are suitable for Jahn-Teller active ions such as Cu^{2+} and Mn^{3+} [17, 20,27]. The B-sites ($8c$: $\frac{1}{4}$ $\frac{1}{4}$ $\frac{1}{4}$), where titanium is substituted by ruthenium, are octahedrally coordinated by oxygens ($24g$: x y 0, where x is typically 0.18 and y is 0.31) [17,28]. This structure type was first described for $CaCu_3Ti_4O_{12}$ in Ref. [29], which is very well known for its outstanding dielectric properties [2,30,31].

A sketch of the cubic $AA'_3B_4O_{12}$ crystal structure is shown in Fig. 1. The close relationship to perovskites such as $CaTiO_3$ or $SrTiO_3$ is obvious. Green corner sharing

[1] In the original perovskite the A-site has a regular 12-fold oxygen cuboctahedral coordination, while in $AA'_3B_4O_{12}$ the A-site is icosahedrally coordinated.

BO_6 octahedra as well as the turquoise spheres marking A-site cations visualize $2 \times 2 \times 2$ perovskite unit cells [29]. Oxygens are represented by small red spheres. A'-cations are marked by dark blue spheres and the $A'O_4$ square plaquettes are highlighted by yellow A'–O bonds. Obviously, the B–O–B angle deviates distinctly from $180°$ for the perovskite as can be easily seen from the tilting between the octahedra. Due to these structural features a plethora of physical properties can be observed depending on the element composition and a rich field of possible applications is opened. Similar to the original perovskites already small substitutions can lead to significant changes of the physical properties. This is due to the strong correlation of the electrons of the A'- and B-site cations caused by B–O–B and A'–O–B exchange interactions, which mutually can affect each other via the A'–O–B–O–A' exchange path. Besides the doping of only one site, a co-substitution on both sites A' and B in principle can be performed and should result in even more complex phenomena.

A prototypical result of the Rietveld-refinement is depicted in Fig. 2a for $LaCu_3Ru_{2.25}Ti_{1.75}O_{12}$. The fit quality indicates phase purity of the samples. This high quality is also obtained for the other substitution levels. In Fig. 2b the diffraction patterns (normalized to the intensity of (220) and shifted by a constant value) of $La_yCu_3Ru_xTi_{4-x}O_{12}$ are shown for different Ru concentrations from $x = 0$ at the top to $x = 4$ at the bottom. With this figure we want to document the complete miscibility for the whole concentration range. For some samples with intermediate x very small features at $2\theta \approx 27°$ mark a minor TiO_2 impurity phase well below 1%.

The unit-cell parameter a obtained from Rietveld-analysis of the x-ray diffraction patterns is depicted in Fig. 3 as a function of the Ru-substitution level x (solid red squares). Starting from the titanate ($x = 0$) the cell parameter a strongly increases by roughly $0.03\,\text{Å}$ for increasing x until $La_1Cu_3Ru_{0.33}Ti_{3.67}O_{12}$. The steep slope is mainly due to the increasing filling of the deficient A-sites (indicated by the occupancy y), but it is also caused by the Ru substitution. The Ru^{4+} ions possess a slightly larger ionic radius compared to Ti^{4+} [32] leading to a monotonous increase of a in agreement with Vegard's law. At $x = 0.33$ the A-site is fully occupied and, therefore, the slope in the substitution range $0.33 \leq x \leq 4$ of the increasing cell edge becomes smaller, since only Ru substitution occurs in this substitution range. The solid line is added to the figure to guide the eye. The data follow the cell parameter values of $NdCu_3Ru_xTi_{4-x}O_{12}$ shown in Ref. [33], they are only larger by a constant amount according to the larger ionic radius of La^{3+} compared to Nd^{3+} [32]. The cell parameters of the samples containing 5% Gd on the La-site are represented by open blue circles. Only minor deviations are caused by the insertion of smaller Gd^{3+} ions, which allows the consideration of constant structural properties at the same ruthenium concentration x as for the undoped samples [21].

4 Magnetic properties

The magnetic susceptibilities of selected $La_yCu_3Ru_xTi_{4-x}O_{12}$ samples are depicted in Fig. 4a for $x = 0$, $x = 2$, and $x = 4$. These are prototypical representatives for the three types of observed susceptibilities.

For the pure titanate ($x = 0$) antiferromagnetic order of the Cu $S = 1/2$ moments below roughly $25\,\text{K}$ is indicated by a distinct anomaly, while up to $400\,\text{K}$ the paramagnetic behavior is well described by a Curie-Weiss law with a Curie-Weiss temperature of $-32\,\text{K}$ and a paramagnetic effective moment of $3.4\ \mu_B$ per formula unit. The resulting average effective moment of $1.99\ \mu_B$ per copper ion is about 15% higher than expected for $S = 1/2$ in spin-only approximation ($1.73\ \mu_B$) indicating an enhanced g value of ≈ 2.23 as often observed in Cu compounds and in satisfactory agreement with $g = 2.16$ as determined from electron spin resonance in polycrystalline
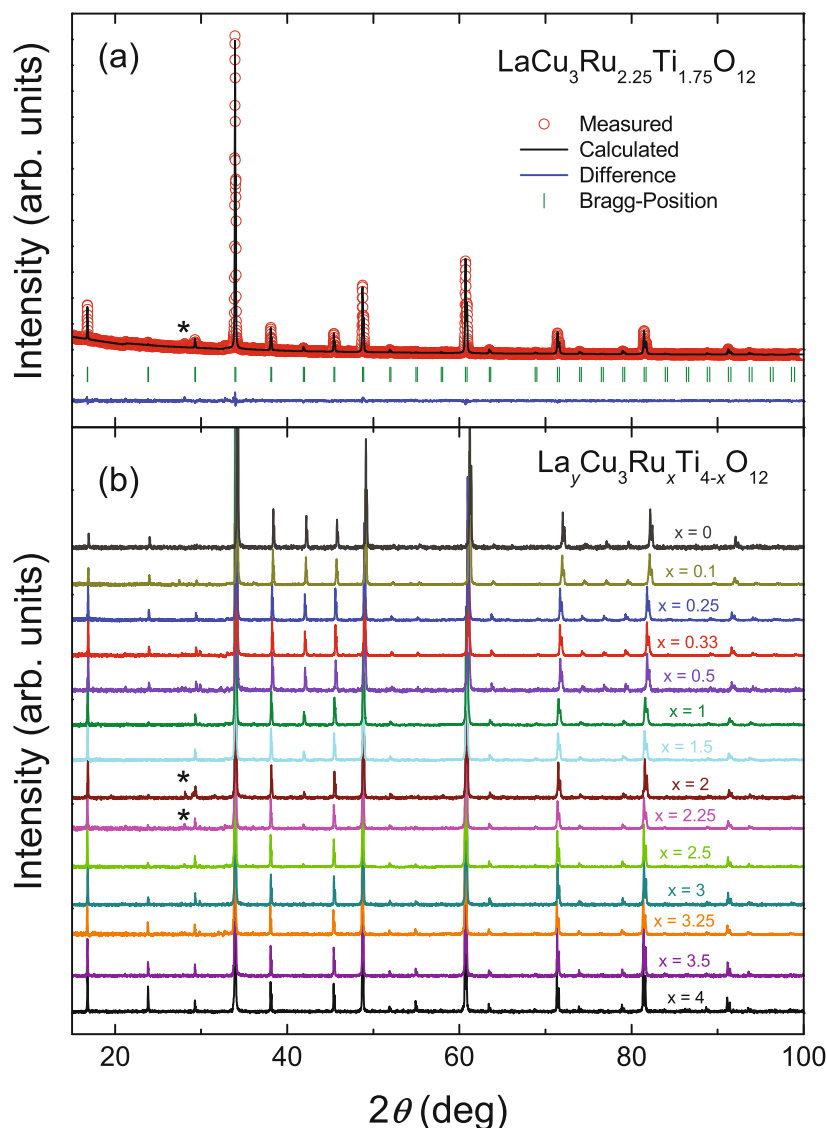
Fig. 2. (a) Representative Rietveld-refinement of the x-ray diffraction pattern of $LaCu_3Ru_{2.25}Ti_{1.75}O_{12}$ measured at room temperature. (b) X-ray diffraction patterns of $La_yCu_3Ru_xTi_{4-x}O_{12}$ for different Ru concentrations x, normalized to the intensity of (2 2 0). Impurity peaks are marked by asterisks.

material [34]. The antiferromagnetic order is also observed for low Ru concentrations and its evolution is shown in Fig. 4b. Rounded cusps indicate long-range magnetic order up to Ru concentrations of $x = 0.33$. For $x \geq 0.5$ the slight kink in the susceptibility has been identified as transition into a spin-glass phase as will be discussed below.

At intermediate concentrations, over wide temperature regions, the magnetic susceptibility cannot be described by a simple Curie-Weiss law as evident from Fig. 4c. Here in the $1/\chi$ representation a curved susceptibility is shown for $x = 1$ and 2 and only at high temperatures a Curie-Weiss susceptibility and a paramagnetic effective
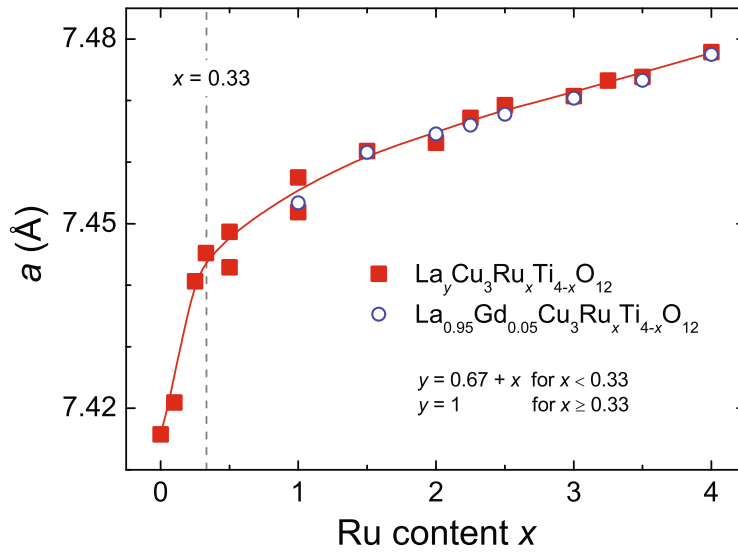
Fig. 3. Cell parameter a of $La_yCu_3Ru_xTi_{4-x}O_{12}$ (solid red squares) obtained from Rietveld-analysis of x-ray diffraction patterns. The solid line is drawn to guide the eye. The Gd doped samples (open blue circles) are prepared for the ESR experiments (see Sect. 7), where Gd^{3+} serves as the local probe.

moment can be deduced from the data. Such a curved susceptibility indicates a distribution of Curie-Weiss temperatures due to microscopic spatial fluctuations of the Ti:Ru ratio. Similar effects are known, e.g. from diluted magnetic semiconductors, where antiferromagnetic clustering between randomly adjacent magnetic ions is responsible for the deviations from the pure Curie-Weiss law at low temperatures [35–38].

The susceptibilities for high Ru substitution levels $x \geq 3$ show a different behavior, since they are only weakly temperature dependent over a wide range. The Curie-like increase of the susceptibility at lowest temperatures indicates the existence of free spins, most likely in grain boundaries. Nevertheless, at elevated temperatures a distinct Curie-Weiss behavior with effective moments of $6\mu_B$ compatible with low-spin Ru^{4+} and partly rather enhanced Curie-Weiss temperatures of up to -800 K can be deduced from a linear fit of the inverse susceptibility data as illustrated in Fig. 4d. These extremely large Curie-Weiss temperatures of the Ru-rich compounds without observable magnetic order down to the lowest temperatures can only be explained in terms of a Kondo-like behavior of a strongly correlated electron system, where the characteristic temperature T^*, indicating the onset of correlations, is of the order $T^* = \Theta_{CW}/4$ [39]. This characteristic temperature is comparable to the temperature of the susceptibility maximum observed in the related compound $CaCu_3Ru_4O_{12}$, which exhibits intermediate valence properties [9]. Below T^* the local magnetic moments of Ru^{4+} appear to be screened by hybridization with the conduction electrons.

The detailed evaluation of different parts of the inverse susceptibility in the full concentration range provides further insight into the evolution of Cu and Ru moments. At first, the high-temperature (hT) part ($T \geq 300$ K) of $1/\chi$ was fit using a standard formula $\chi = C/(T - \Theta_{CW})$ representing the Curie-Weiss law (dashed line). The obtained effective magnetic moments (μ_{eff}) and Curie-Weiss temperatures (Θ_{CW}) are depicted as solid blue circles in Fig. 5. The theoretical values of the sum of Cu^{2+} and Ru^{4+} spin moments according to $\mu_{eff} = \sqrt{3 \cdot \mu_{eff}^2(Cu^{2+}) + x \cdot \mu_{eff}^2(Ru^{4+})}$ is shown
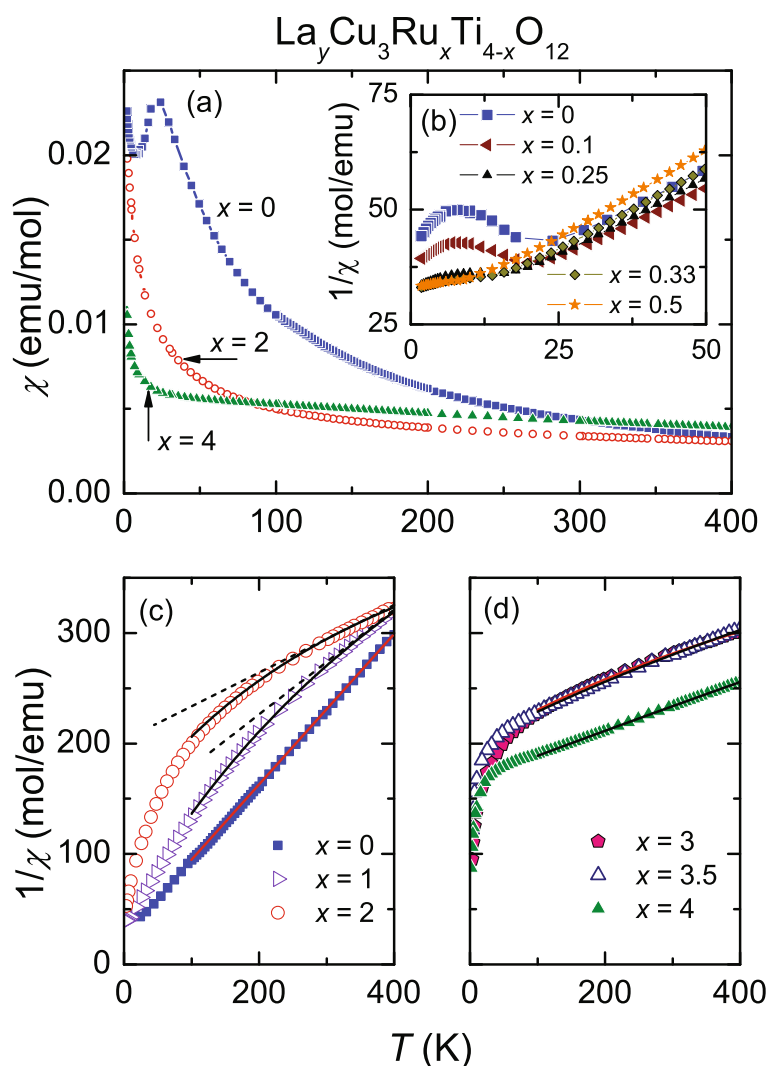
Fig. 4. (a) Temperature dependent magnetic susceptibility $\chi(T)$ of $La_yCu_3Ru_xTi_{4-x}O_{12}$ for selected substitution levels x. The inverse susceptibilities are shown in panels (b), (c), and (d) for $x \le 0.5$, for $x = 0$, 1, and 2, and for $x \ge 3$, respectively. Fits are shown as dashed lines for the "hT-fits" and solid lines for the "best fits".

as dashed black line in Fig. 5a. The obtained fit values are satisfactorily following these theoretical values indicating stable local Ru spin moments in this temperature range. The Curie-Weiss temperatures are constant below $x = 1$ at roughly $-100\,\mathrm{K}$ and decrease monotonously to a minimum of $-1100\,\mathrm{K}$ for $x = 3$. For $x > 3$ the values increase again to approximately $-800\,\mathrm{K}$.

By adding a temperature independent correction term χ_0 representing a Pauli susceptibility, as expected in conventional metals, and possible van-Vleck paramagnetic terms, the fit equation transforms to $\chi = C/(T - \Theta_{CW}) + \chi_0$. Using this expression the experimental data can be satisfactorily approximated in the temperature range $100 \le T \le 400\,\mathrm{K}$. This was denoted "best fit", since the deviations of the fit over the complete temperature range are rather small. For the effective magnetic moments
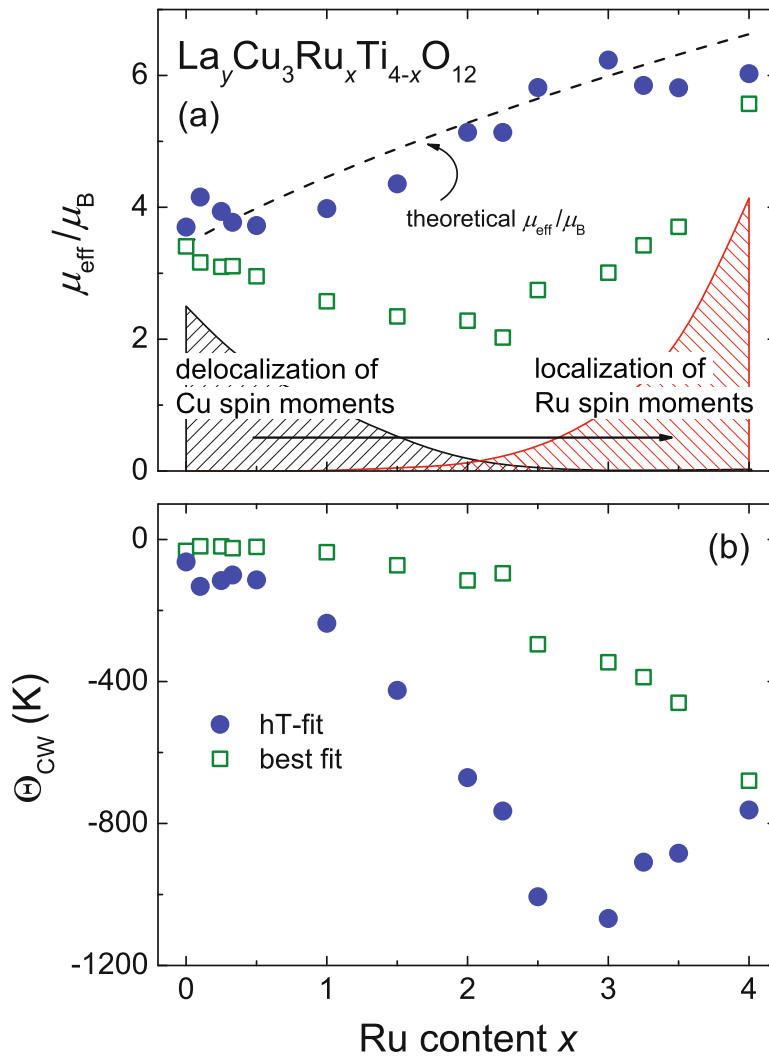
Fig. 5. (a) Effective magnetic moment μ_{eff} of $La_yCu_3Ru_xTi_{4-x}O_{12}$ obtained from Curie-Weiss fits of the inverse magnetic susceptibilities for different temperature intervals. The dashed black line marks the theoretical sum of Cu^{2+} and Ru^{4+} spin moments. For the "best fit" data the shaded areas represent the corresponding change of the spin moment per Cu or Ru ion as obtained from DFT calculations, see Fig. 13. The lower arrow indicates the direction in x of increasing delocalization or localization of spin moments. For details see text. (b) Corresponding Curie-Weiss temperatures Θ_{CW} obtained from the Curie-Weiss fits.

(Fig. 5a, open green squares) an unexpected evolution is observed. A minimum is found at $x \approx 2$ and the experimental values are strongly deviating from the theoretical sum of the spin-only values for intermediate values of x. The reason is that this kind of evaluation provides stronger weight to Curie-Weiss contributions with small negative values of the CW temperature, while those with large negative CW temperature are primarily covered by the temperature-independent contribution. This is also evident from the obtained CW temperatures with their absolute values generally smaller than those of the hT-fit (Fig. 5b). Up to $x = 2$, the values change only weakly

from about $\Theta_{CW} \approx -20\,K$ to $-100\,K$ with increasing x, while they shift from $-100\,K$ to $-700\,K$ in the range $2 \leq x \leq 4$. In spite of these discrepancies at intermediate Ru concentrations, for the parent compounds ($x = 0$ and $x = 4$) both approaches yield approximately the same effective moments and CW temperatures. We conclude that whilst at high temperatures the effective moment of the spin-only values of Cu and Ru are recovered, at low temperatures hybridization and Kondo-like screening effects play a dominant role.

Besides the evolution of effective moment and Curie-Weiss temperature, measurements of the field-cooled (FC) and zero-field-cooled (ZFC) susceptibility suggested a spin-glass phase in the concentration range $0.5 \leq x \leq 2$ by a distinct splitting between FC and ZFC branches as illustrated in Fig. 6a. $LaCu_3RuTi_3O_{12}$ ($x = 1$) exhibits this behavior most clearly with a sharp cusp in the real part of the AC-susceptibility at the freezing temperature T_f defined as the maximum in χ'. To provide experimental evidence for the occurrence of a spin-glass state for $x \leq 2$, we performed a series of detailed AC-susceptibility measurements. Some representative results of these AC-susceptibility measurements with an AC-field of 2 Oe and measuring frequencies in the range $1.3 \leq \nu \leq 1120$ Hz are also shown in Fig. 6a for $LaCu_3RuTi_3O_{12}$. The investigated samples show a frequency dependent shift of the freezing temperature in the real part of the AC-susceptibility. In Fig. 6a the peak at roughly $8\,K$ is shifting to lower temperatures with decreasing frequency, the typical behavior of canonical spin glasses [41,42].

In Fig. 6b the obtained freezing temperatures T_f from the maxima for $LaCu_3RuTi_3O_{12}$ are depicted in an Arrhenius-plot. The measuring frequencies determine the relaxation times $\tau = 1/(2\pi\nu)$ plotted on a logarithmic scale. The values follow a typical Arrhenius behavior in this small temperature range, which is marked by the solid line. Due to the small temperature range an energy barrier of $\Delta \approx 100$ meV together with an unphysically high attempt frequency is obtained from the fit. Nevertheless, this indicates a thermally activated behavior for the spin-glass state. It has to be mentioned that the Arrhenius behavior is only clearly observable for $x = 1$, because the frequency dependent shift of the cusp maxima is significantly smaller for other substitution levels, though it is visible for $0.5 \leq x \leq 2$. On the other hand, for $x > 2$ neither an FC-ZFC splitting nor a cusp in the AC-susceptibility were observed.

The evolution of the magnetic properties for increasing ruthenium content x can only be explained by the electronic correlations in $La_yCu_3Ru_xTi_{4-x}O_{12}$, the changing Cu valence and the gradual delocalization/localization of the Cu/Ru valence electrons. The AFM order of the Cu spin moments in the pure titanate was described by ferromagnetically coupled Cu moments in the {111}-planes, which are antiferromagnetically coupled with each other resulting in the negative Curie-Weiss temperature [40]. This ordering should be influenced by the Ru substitution, since the Ru ions (with d electrons) are inserted into the main exchange path Cu–O–B–O–Cu (B = Ti, Ru) between the planes. This is evidenced from the monotonously decreasing B–O–B bonding angle (from $\approx 141°$ for $x = 0$ to $\approx 139.5°$ for $x = 4$), while the Cu–O–B angle remains constant at approximately $109.5°$. Indeed, as will be shown later by band-structure calculations, the Ru substitution gives rise to gradual delocalization of the Cu valence electrons up to $x = 2$, where the spin-glass phase is suppressed, and builds up localized Ru moments for higher x which become screened by the delocalized copper electrons resulting in the paramagnetic heavy-fermion ground state at low temperatures. This behavior is qualitatively reflected by the "best fit", which indicates first the decrease of the local copper moments at intermediate temperatures up to $x = 2$ and then the increase of the local ruthenium moment for larger x.
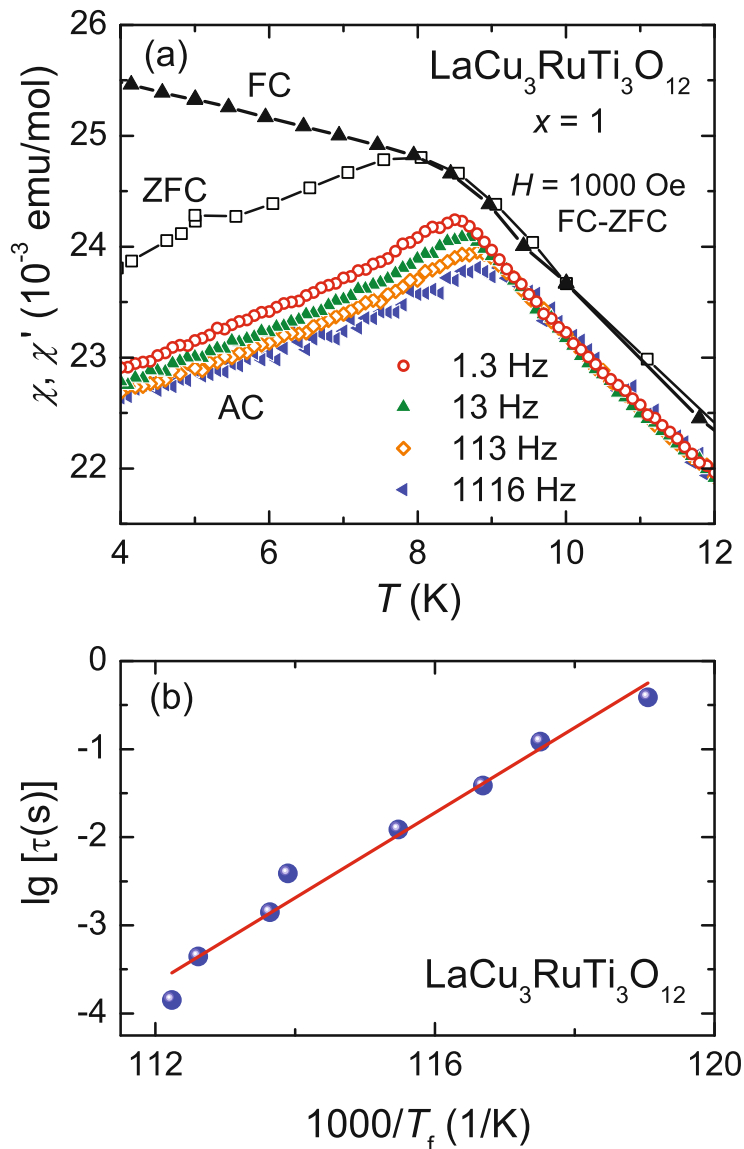
Fig. 6. (a) Field-cooled (FC) and zero-field cooled (ZFC) susceptibility of $LaCu_3RuTi_3O_{12}$ ($x = 1$) measured at $H = 1000$ Oe. AC–susceptibilities χ' are also shown for different frequencies. (b) Arrhenius plot of the relaxation time $lg[\tau]$ versus the inverse freezing temperature T_f for $LaCu_3RuTi_3O_{12}$. The solid line is a linear fit indicating the Arrhenius-like behavior.

5 Thermodynamic properties

For further characterization we performed heat-capacity experiments for the entire ruthenium concentration range. As an example, Fig. 7 shows the heat capacity of $La_{2/3}Cu_3Ti_4O_{12}$ from 2.2 K up to room temperature in a representation of C/T as a funcion of T. A lambda-shaped anomaly is clearly visible close to 22 K indicating the transition into long-range antiferromagnetic order of the Cu spin moments as observed in the magnetic susceptibility. This magnetic contribution is on top of the typical
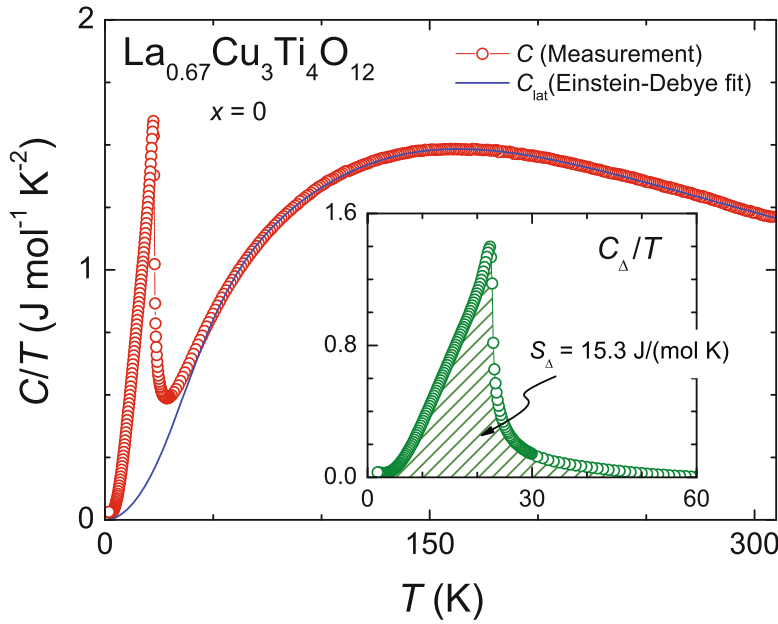
Fig. 7. Specific heat of $La_{2/3}Cu_3Ti_4O_{12}$ in $C(T)/T$ representation. The corresponding Einstein-Debye phonon fit is shown as solid line. In the inset the residual magnetic heat capacity C_Δ/T after subtraction of the phonon fit is depicted. The magnetic entropy S_Δ (shaded area) amounts to $15.3\,\mathrm{J\,mol^{-1}\,K^{-1}}$.

phononic heat capacity C_{lat} of the crystal lattice which can well be described by an Einstein-Debye model (solid line in Fig. 7). To model the phononic heat capacity, one Debye and several Einstein terms are required, each defined by its characteristic Einstein- or Debye-temperature Θ_E or Θ_D. If we subtract the phonon contribution, the pure magnetic heat capacity $C_\Delta = C - C_{lat}$ is obtained. C_Δ/T is shown in the inset in Fig. 7 for $2.2 \leq T \leq 60\,\mathrm{K}$ and the lambda shape typical for a second-order phase transition at T_N becomes clearly observable. To obtain the magnetic entropy change of this transition, C_Δ/T is integrated over temperature: $S_\Delta = \int C_\Delta/T\ \mathrm{d}T$. This is marked by the shaded area under the peak in the inset of Fig. 7.

In Fig. 8 we show the low-temperature part ($T \leq 30\,\mathrm{K}$) of the specific heat for selected Ru contents x. The heat capacity of the higher temperature range is basically identical for all compounds due to the dominant phononic contribution and therefore is not shown. The lambda-type anomaly indicating the antiferromagnetic (AFM) ordering transition is observable for $x \leq 2$, but becomes smeared out and shifted to lower temperatures for increasing x. The cusp-like shape of the transition persists up to a value of $x = 0.33$, while for $x > 0.33$ the AFM ground state evolves into a spin-glass state with a smoothed maximum in C_Δ/T. Already for values of $x \geq 2.25$ no sign for any magnetic transition at low temperatures is observable, however, the extrapolation of C/T towards zero temperature is clearly enhanced. This indicates an additional electronic contribution to the specific heat which is usually denoted as Sommerfeld-coefficient. Since this contribution is directly linked to the number of free electrons at the Fermi-level, this behavior is typical for a metal. The samples exhibit considerably increased Sommerfeld-coefficients of up to $139\ \mathrm{mJ/mol\,K^2}$ for $LaCu_3Ru_4O_{12}$ [18]. This increase was also reported for spin-glasses, but with much lower Sommerfeld-coefficients. Nevertheless, due to this it becomes rather difficult to
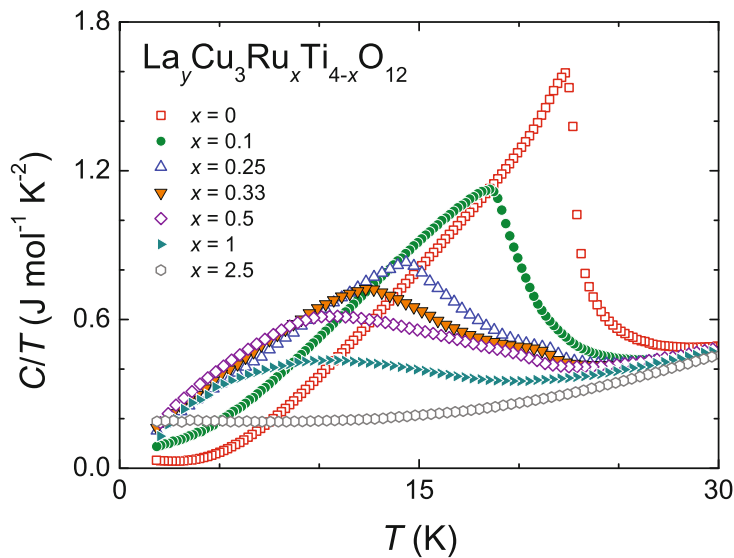
Fig. 8. Detail of the specific heat in C/T representation of $La_yCu_3Ru_xTi_{4-x}O_{12}$ for selected Ru concentrations in the range $T \leq 30\,\mathrm{K}$.
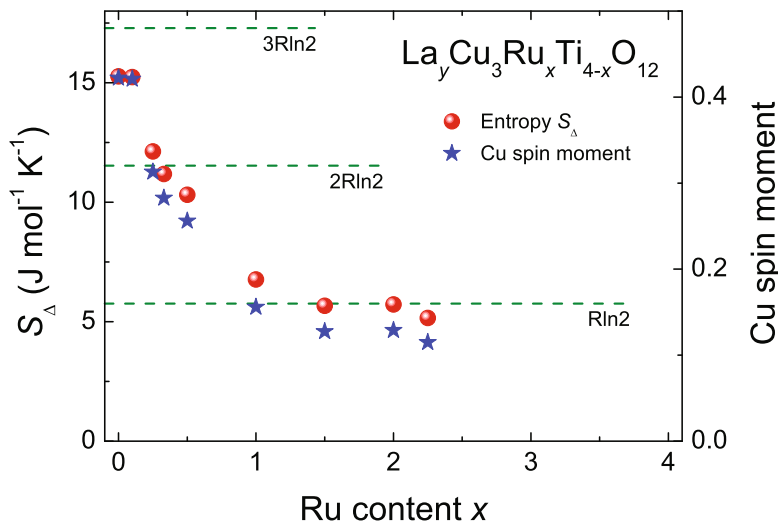
Fig. 9. Magnetic entropy S_Δ obtained from the integration of the magnetic heat-capacity contribution shown in Fig. 8 (solid red spheres, left scales) and the from these values calculated corresponding Cu spin moments (stars, right scales).

obtain the pure magnetic fraction of the heat capacity already for the spin-glass phase of $La_yCu_3Ru_xTi_{4-x}O_{12}$.

The magnetic entropies obtained from the residual heat capacity after subtraction of the phonon contribution is shown in Fig. 9 for $0 \leq x \leq 2.25$. Theoretically one expects that AFM order results in an entropy change of $S_\Delta = \mathrm{Rln}(2S+1)$ per divalent copper ion with $S = 1/2$. Using this relation the average copper spin moments (shown as stars in Fig. 9) were calculated according to $1/2 \cdot [\exp{(S_\Delta/3R)} - 1]$. The experimentally determined entropy for $x = 0$ amounts to $15.3\,\mathrm{J\,mol^{-1}\,K^{-1}}$ and is only slightly lower than the expected value of $3\mathrm{R}\ln 2 = 17.3\,\mathrm{J\,mol^{-1}\,K^{-1}}$. Hence,
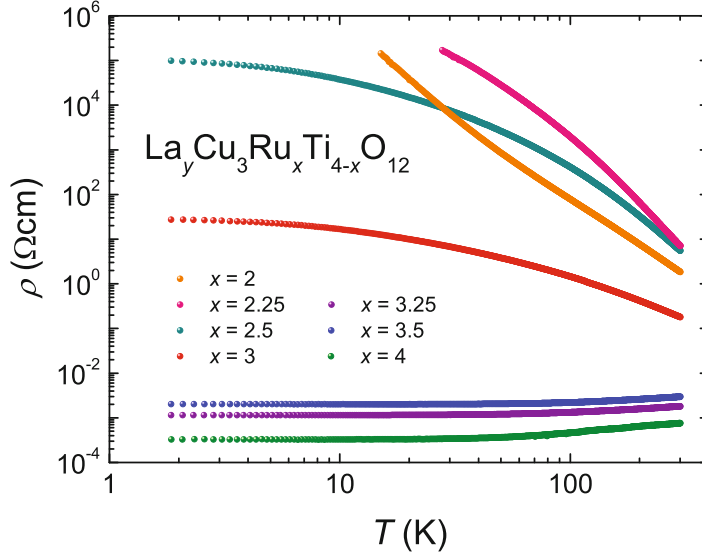
Fig. 10. Temperature-dependent electric resistivity $\rho(T)$ of $La_yCu_3Ru_xTi_{4-x}O_{12}$ for ruthenium contents $2 \leq x \leq 4$ and La occupancies $y = 1$.

the average spin moment per copper ion amounts to 0.41, which is somewhat smaller than the expected spin $S = 0.5$ but comparable to the results of the DFT calculations discussed in Sect. 8. For the other samples the calculated spin moments decrease with increasing x according to the smaller cusps observed in the low temperature specific heat. This indicates a beginning delocalization of the copper $3d$ electrons with increasing Ru concentration and a smaller average local Cu spin moment. The lowest spin values obtained for $x = 2$ and $x = 2.25$ have to be considered with caution, since for these samples the electronic contribution of the specific heat becomes comparable to the magnetic one. Therefore, a correction using an appropriate Sommerfeld-coefficient would be expected to lower the spin values significantly below $S = 0.1$ indicating the itineracy of the Cu electrons and the proximity of the metal-to-insulator transition.

6 Transport properties

Figure 10 depicts the temperature dependence of the electrical resistivity $\rho(T)$ obtained in $La_yCu_3Ru_xTi_{4-x}O_{12}$ for $2 \leq x \leq 4$ on a double logarithmic scale, as the values develop over ten orders of magnitude $10^{-4} < \rho < 10^6$ Ωcm. For lower ruthenium contents $x < 2$ the conductivities were too low to achieve reasonable data with the applied experimental setup. At $T = 300$ K the absolute value of the resistivity generally increases on decreasing x except for $x = 3.25$ and $x = 2$, which appear to be lower than expected. This most likely results from the fact that the resistivity measurements have been performed on pressed powder samples, which naturally leads to a scattering of the absolute values. Nevertheless, the development of the resistivity with temperature is unequivocally linked to the ruthenium content.

Starting from $x = 4$ the samples with $3.25 \leq x \leq 4$ exhibit a clear metallic behavior where the resistivity decreases on decreasing temperature. A closer analysis reveals a quadratic temperature dependence $\rho = \rho_0 + AT^2$ which is typical for heavy-fermion compounds, where the mass enhancement allows detecting the contribution of electron-electron scattering, which otherwise is too weak to be observable and,

hence, masked by the $\rho_{\mathrm{ph}} \propto T^5$ low-temperature phonon-scattering contribution. For LaCu$_3$Ru$_4$O$_{12}$ a value of $A = 15.4$ nΩcm/K^2 is obtained [18] which is comparable with the result published by Tanaka et al. in Ref. [6]. For intermediate ruthenium concentrations $2.25 \leq x \leq 3$ the metallic characteristics breaks down and the resistivity increases on decreasing temperature. However, the temperature dependence is not really semiconducting either, because the data do not diverge towards low temperatures. For $x = 3$ the resistivity even increases only by two orders of magnitude when lowering the temperature from $300\,$K to $2\,$K. Only for $x \leq 2$ the resistivity actually diverges at very low temperature as expected for a semiconductor or insulator.

To understand the behavior in the intermediate range, we have to consider the effect of dilution of the ruthenium sublattice by titanium. As corroborated by the magnetic-resonance experiments presented in the following section, Ru^{4+} with its magnetic moment hybridizing with the conduction electrons, is responsible for the heavy-fermion formation. On dilution of Ru^{4+} with non-magnetic Ti^{4+}, the heavy Fermi liquid is weakened, until its coherence breaks down for $x = 3$. However, the hybridization is locally still present, now enhancing the resistivity to low temperatures due to scattering of the conduction electrons at the Ru^{4+} spins. This is comparable to the scenario observed on dilution of dense $4f$-electron based Kondo-lattice compounds developing from a coherent Fermi-liquid state to the single-ion Kondo effect such as reported for Ce$_x$La$_{1-x}$Cu$_{2.05}$Si$_2$ [43]. Note, however, that in contrast to those $4f$ systems, in LaCu$_3$Ru$_x$Ti$_{4-x}$O$_{12}$ the absolute increase of the resistivity to low temperatures is much stronger, because on dilution the conduction electrons tend to localize at the copper sites such that the conductivity gradually decreases and in turn the single-ion Kondo-like behavior transforms into a purely semiconducting characteristics for $x \leq 2$.

7 Magnetic resonance

Electron spin resonance (ESR) and nuclear magnetic/quadrupole resonance (NMR/NQR) are local methods, which probe the electronic properties on a microscopic level. For example, in heavy-fermion compounds these contact-free techniques yield precise information on the local distribution of the electronic mass enhancement in the Fermi-liquid regime, on the opening of excitation gaps at the onset of antiferromagnetic order, or on non-Fermi-liquid behavior close to a quantum-critical point [44–47]. Our previous NQR experiments performed on the ^{101}Ru and ^{63}Cu nuclei in CaCu$_3$Ru$_4$O$_{12}$ successfully established the formation of heavy effective-electron masses at the ruthenium site as well as even reduced effective masses and non-Fermi-liquid behavior at the copper site [5,9,18]. In case of NQR we have the advantage to be able to study the unperturbed system, as we excite RF transitions between the nuclear quadrupole levels naturally split by the intrinsic electric-field gradient (EFG) and, therefore, we do not have to apply any external magnetic field as is necessary in case of NMR or ESR.

In LaCu$_3$Ru$_4$O$_{12}$ we found a ^{63}Cu-NQR signal comparable to that in CaCu$_3$Ru$_4$O$_{12}$, but we could not detect any useful signal of the ^{101}Ru nuclei neither by NQR nor by NMR. Moreover, by means of ESR we did not succeed to find traces of electronic copper or ruthenium magnetic resonances in this sample. Hence, we followed the procedure usually applied in $4f$- and $5f$-electron based intermetallic compounds and doped a few percent of gadolinium on the lanthanum site [48]. Gd^{3+} exhibits an electron configuration $4f^7$, i.e., a half-filled $4f$ shell and stable spin-only $S = 7/2$ state with a g-value $g = 2$. Due to vanishing orbital momentum the direct spin-lattice relaxation is negligible and the relaxation via the conduction electrons becomes dominant, which makes gadolinium a powerful local probe in metals.
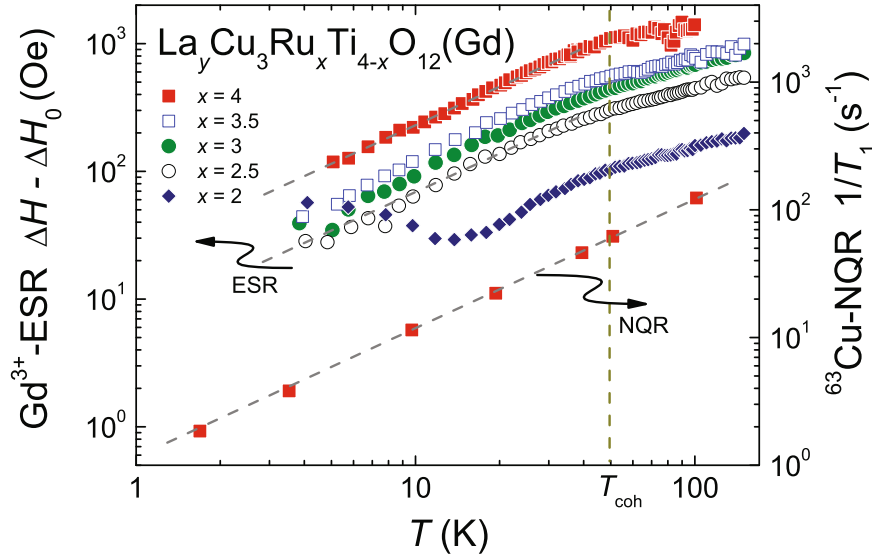
Fig. 11. ESR line width $\Delta H - \Delta H_0$ and NQR spin–lattice relaxation rate $1/T_1$ versus temperature on a double-logarithmic scale. Shown are Ru substitution values x from the metallic part of the phase diagram. The straight lines indicate the linear Korringa relation, i.e. $\propto T$. T_{coh} is the coherence temperature of the Kondo system.

In $La_{0.95}Gd_{0.05}Cu_3Ru_4O_{12}$ the Gd^{3+}-ESR signal consists of a single exchange-narrowed asymmetric Lorentz line which is typical for metals because of the skin effect which admixes contributions of dispersion into the absorption [49]. For the substitutional series $La_{0.95}Gd_{0.05}Cu_3Ru_xTi_{4-x}O_{12}$ the spectrum becomes more and more symmetric on decreasing x, resulting from decreasing conductivity on approaching the metal-to-insulator transition. Simultaneously, deviations from the ideal Lorentz shape become significant for $x \leq 2$ indicating insufficient exchange narrowing due to a lack of conduction electrons in the insulating regime. Thus, the ESR line shape turns out to be a sensitive indicator of the metal-to-insulator transition close to $x = 2$ [21].

Selected comparative results of our ESR and NQR experiments are shown in Fig. 11, which depicts the longitudinal spin-relaxation rates $1/T_1$ obtained by both methods. While in NQR the relaxation rate $1/T_1$ is directly measured by pulse methods, it is extracted from the half-width-at-half-maximum (HWHM) line width of the CW-ESR signal by subtraction of a temperature-independent residual line width ΔH_0 (due to inhomogeneities and impurities) such that the extrapolated width $\Delta H - \Delta H_0$ vanishes at $T = 0$. After subtraction the remaining relaxation contribution $\Delta H - \Delta H_0$ can be considered to represent the longitudinal ESR relaxation rate $1/T_1$, although the line width strictly resembles the transverse relaxation rate $1/T_2$, because in metals usually $T_1 = T_2$ holds [49].

In the double-logarithmic plot of Fig. 11 the metallic Korringa relaxation $1/T_1 = b \cdot T$ due to the scattering of conduction electrons at the ^{63}Cu-nuclear spin or Gd^{3+}-electron spin corresponds to a straight line with a slope of 1 as indicated by the dashed grey lines. In conventional metals the factor $b \propto N^2(E_F)$ depends on the squared density-of-states at the Fermi energy $N(E_F)$, but becomes enhanced in a heavy-fermion metal below its characteristic temperature T^* by an additional contribution proportional to the Pauli-like paramagnetic susceptibility χ_{HF} of the ions responsible for the heavy-fermion formation. Regarding the ^{63}Cu-NQR relaxation rate in $LaCu_3Ru_4O_{12}$, we obtain a linear temperature dependence, with its absolute

value $^{63}b \approx 1 \ \mathrm{s}^{-1}\mathrm{K}^{-1}$ comparable to that observed in copper metal [50]. In contrast to $CaCu_3Ru_4O_{12}$ there is no hint for any non-Fermi-liquid behavior at the Cu site. The Cu nuclear spin is also not sensitive to the electronic mass enhancement.

On the other hand, the Gd-ESR line width of $LaCu_3Ru_4O_{12}$ exhibits a considerable linear increase $b_{LT} \approx 24 \ \mathrm{G/K}$ for $T \leq 50 \ \mathrm{K}$. This slope is larger than the one found for usual metals of about $b \approx 5 \ \mathrm{G/K}$ [51]. Above $\approx 50 \ \mathrm{K}$ the line-width $\Delta H(T)$ obviously increases with a smaller slope. This border of changing slopes is marked by the coherence temperature T_{coh}, the upper temperature limit of the Fermi-liquid regime [52,53]. Below T_{coh} typically a linear behavior is observed for heavy fermions which is followed by a nonlinear regime and finally approaches a moderate Korringa law at high temperatures above the characteristic $T^* \gg T_{\mathrm{coh}}$ [54]. From this it is evident that Gd-ESR is capable to measure the electronic mass enhancement at the ruthenium ions similarly to ^{101}Ru-NQR in $CaCu_3Ru_4O_{12}$ [9]. With decreasing Ru content the temperature dependence of the gadolinium line width is still linear but with monotonously decreasing slope b_{LT} down to 7.5 Oe/K for $x = 2.5$ due to Ru dilution. Reaching $x = 2$ no real linear behavior is discernible anymore signaling the crossover to the insulating regime. From the extrapolation of the line width any residual Korringa contribution at high temperatures would be at least less than 1 Oe/K. Approaching the spin-glass state the line width even increases at low temperatures.

Thus, the metal-to-insulator transition in $La_yCu_3Ru_xTi_{4-x}O_{12}$ is characterized just by a fading of the metallic spin relaxation contributions without any critical divergence. This is different from the behavior observed earlier in $Gd_{1-x}Sr_xTiO_3$ [55,56], where the heavy-fermion type relaxation contribution diverges on approaching the insulating regime due to diverging effective electronic masses, which has been also observed in specific-heat measurements on the related compounds $La_{1-x}Sr_xTiO_3$ and $Y_{1-x}Ca_xTiO_3$ [57,58]. The basic difference is that in those compounds the lattice of the $3d$-Ti ions remains intact, but substitution only changes the electronic filling on the Ti sites between $3d^0$ and $3d^1$. The $3d$ electrons can move on the Ti lattice and the correlations increase with increasing number of $3d$ electrons, giving rise to enhancing effective masses and finally to the formation of the Mott insulator. In contrast, in $La_yCu_3Ru_xTi_{4-x}O_{12}$, the magnetic Ru^{4+} ions, at which the heavy-fermion formation takes place, are substituted by non-magnetic Ti^{4+} ions with empty $3d$ shells. Therefore, Ti substitution breaks the lattice periodicity of the heavy-fermion system and strongly disturbs the $4d$ band structure. This in turn inhibits the conductivity, while the electronic filling remains unaffected by the substitution.

8 Band-structure calculations

The electronic band structure of the solid-solution series $La_yCu_3Ru_xTi_{4-x}O_{12}$ was studied using density-functional theory (DFT). For $CaCu_3Ti_4O_{12}$ several publications on DFT calculation results can be found in literature. This is reasoned by the observed unusual high dielectric constant of this oxide, which motivated the high interest in the electronic structure. Different approaches were used in the *ab initio* calculations. Local-density-approximation (LDA) as well as local spin-density-approximation (LSDA) were reported in Refs. [59–61]. Other functionals such as the generalized-gradient-approximation were used in Refs. [62,63]. From Hückel crystal-orbital overlap-population models the density-of-states (DOS) was derived in Ref. [64]. The results of the different approaches were compared in Ref. [65]. The most sophisticated LSDA+U calculation results were shown in Ref. [66]. For the ruthenates $ACu_3Ru_4O_{12}$ (A = Na, Ca, Sr, La, Nd) the DOS was obtained using the augmented spherical wave approach as reported in Refs. [67,68]. However, neither calculations

for the $La_{2/3}Cu_3Ti_4O_{12}$ nor for any example of the series $La_yCu_3Ru_xTi_{4-x}O_{12}$ except $x = 4$ were reported so far to our best knowledge, which motivated own DFT calculation studies of several of these compounds.

To model the mixing of Ru and Ti on the B-site in the symmetry reduced $P1$ unit cell, several combinations of Ru and Ti were placed on the eight available sites. Thus, the substitution levels $x = 0.5, x = 1, \ldots, x = 3.5, x = 4$ correspond to the replacement of one, two, ..., seven or eight Ti ions by Ru, respectively. The modelling of varying combinations of the site occupations, which are not equal by a symmetry operation, was required from two to six replaced ions to study the energetical preference of order on the B-site by taking the solution with lowest total energy. By this variation no preference for long-range ordered arrangements was found, i.e. the lowest energies were found for statistically distributed B-sites, not for layered or striped arrangements. This result was expected, since if such highly symmetrical orderings were present, they would be observable by superstructural reflections in the XRD patterns. Nevertheless, all possible combinations neglecting the symmetry equivalent ones were modelled, because the obtained difference to the minimum energy can be used to argue on the probability of the existence of these arrangements averaged over the whole crystal structure. Since the modelled unit cell is only the smallest supercell available for this compound, more sophisticated algorithms generating larger supercells with a random distribution of the B-cations might perhaps lead to more realistic results, but were not available. However, the results already agree very well with the experimental data. It has also to be mentioned that the La-site in $LaCu_3Ti_4O_{12}$ was set as fully occupied. This was required since it was not possible to obtain reasonable results simulating a 2/3rd occupied site with a coherent-potential approximation (CPA) due to the large difference of the "atom" chemical properties, i.e. La and empty site [69]. Thus, the additional positive charge (+1/3 per formula unit) has to be kept in mind mainly causing a slight shift of the band structure relative to E_F.

Due to the only weak correlation between Cu $3d$ and Ru $4d$ electrons in the semiconducting phase the calculations readily converged only up to a maximum substitution level of $x = 2.5$. For $x > 2.5$ the strong correlations in the metallic regime made it necessary to slightly soften the usually sharp condition in variation of the electronic density to achieve convergence of the calculations. This indicates the expected correlation effects observed for heavy-fermion behavior.

Upon using the spin-polarized LSDA the magnetic arrangement of the cationic spin moments can be investigated by different initial spin settings. For $LaCu_3Ti_4O_{12}$ the AFM setting of the Cu spin moments leads to a converging solution providing the local spin moment $S = \pm 0.38$ (the signs indicate the antiparallel arrangement of the spin directions) close to the nominal $S = 1/2$ per divalent copper ion. The obtained magnetic structure shows the same alternation of ferromagnetically ordered layers along the [111]-direction as reported for $CaCu_3Ti_4O_{12}$ [40]. Thus, with respect to the magnetic properties discussed above the Cu spins were all set to this AFM configuration before the LSDA calculations for the Ru substituted samples were started. On the other hand, for the Ru-sites the spin moments were initially set in a ferromagnetic arrangement using a value $S = 1$.

In Fig. 12 the obtained total density-of-states for the calculation result with lowest total energy for integer x are depicted for the energy range -8 to $+3$ eV around the Fermi-energy and marked by grey shaded areas. Only the spin-up channel of the DOS is shown since due to the (apparent) AFM order symmetrical DOS of both majority and minority spin channels are obtained. The DOS of $LaCu_3Ti_4O_{12}$ ($x = 0$) is shown at the bottom and the results for the substitution series with integer x are shown up to $LaCu_3Ru_4O_{12}$ ($x = 4$) at the top. The obtained DOS for $LaCu_3Ti_4O_{12}$ is very similar to the one reported for $CaCu_3Ti_4O_{12}$ (also using LSDA) except for the shift relative to E_F by approximately -0.3 eV [60,61]. The general shape in the
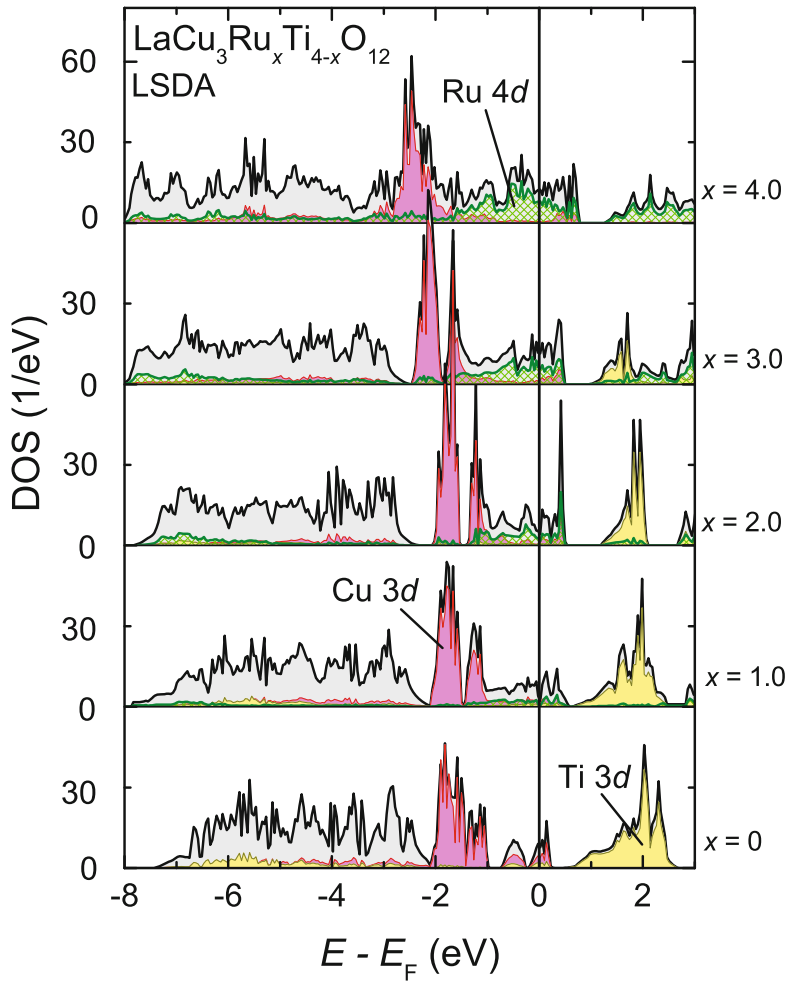
Fig. 12. Total density-of-states DOS (grey) of $LaCu_3Ru_xTi_{4-x}O_{12}$ obtained by DFT-calculations using LSDA (only spin-up channel is shown) for integer values of x. The partial DOS of Cu 3d and Ti 3d are colored red and yellow. For the ruthenium 4d bands the partial DOS is marked by the green cross-shaded area.

vicinity of E_F of $CaCu_3Ti_4O_{12}$ was also evidenced by measurements of the optical conductivity [70]. The Ti 3d bands found above 1.5 eV are colored yellow. Between -1 and 0.5 eV small contributions of the Cu and Ti 3d bands are located. These states could be shifted to higher energies resulting in a realistic band gap of this insulating phase using an additional Hubbard-U term, such as described in Ref. [66]. The Cu 3d bands are colored red and form a broad peak around -1.5 eV. The remaining part is dominated by the large number of oxygen 2p bands merely reflecting the gray shaded area. The Ru 4d bands (green cross shaded area) appear mainly between -2 and $+0.5$ eV around the Fermi energy starting with $x = 0.5$. As expected the Ru 4d contributions increase with increasing substitution level, while the partial DOS of Ti 3d decreases in accordance with the substitution level x. Especially at E_F the enhanced number of Ru 4d bands close the band gap, which is existing for $x = 0$, and a higher electrical conductivity can be expected. This can also be derived from the
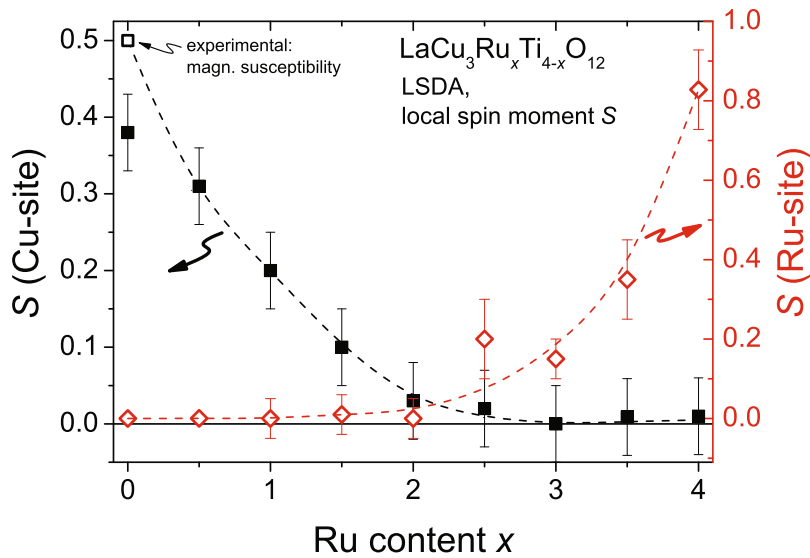
Fig. 13. Local average spin moments of Cu (solid black squares) and Ru (open red rhombes) in $LaCu_3Ru_xTi_{4-x}O_{12}$ obtained by DFT calculations using LSDA. The Cu moments are found to be antiferromagnetically arranged, while the Ru moments show no preference to order. For $x = 0$ the spin-moment value for the copper ions obtained from the magnetic susceptibility data is shown in addition as empty black square.

change of the sample color from brownish to black as soon as a small amount of Ru is substituting Ti and from the resistivity data discussed in Sect. 6.

The sharply peaked Ti $3d$ pDOS above 0.5 eV is only slightly shifted upon Ru substitution. On the other hand, for $x \geq 2.5$ the DOS in this region is smeared out to a broad structure reflecting the Ru $4d$ e_g bands of the RuO_6 octahedra. The whole broad peak structure of the main contribution of the Cu $3d$ bands located between -2 and -1 eV in the valence band is shifted gradually with increasing x by roughly -1 eV in $LaCu_3Ru_4O_{12}$ compared to the titanate[2]. The shift is rather small for $x \leq 2.5$ but is visibly enhanced for higher Ru concentrations. This finding correlates with the decrease of the Cu valence observed by x-ray absorption near edge structure (XANES) spectroscopy [19]. In general, the total DOS becomes significantly broadened and smoothened upon the increasing ruthenium concentration indicating the increasing delocalization of the Cu $3d$ electrons in the system in accordance with the results discussed in the previous sections.

Local spin moments of the ions on the Cu- and Ru-sites are additionally obtained from the DFT calculations. The averaged moments for Cu and Ru versus the substitution level are depicted in Fig. 13. The Cu spin values decrease gradually from approximately 0.38 for $x = 0$ to almost zero for $x \geq 2.5$. This finding is in agreement with the Cu spin moments obtained from the entropy values derived from the experimental specific-heat data (Sect. 5) as well as with the qualitative evolution of the effective moment derived from the "best fit" of the susceptibility data (Sect. 4). For $x = 0$ the value $S = 0.5$ is more realistic, since it was obtained from the magnetic susceptibility data and the above mentioned deviation of the La-site occupation surely influences the value found in the DFT calculation. In contrast to the copper moments, the local Ru spin moment increases for $x \geq 2.5$ again in good qualitative

---

[2] For which to be correct the whole DOS must be shifted to higher energies due to the used $LaCu_3Ti_4O_{12}$ formula unit instead of $La_{2/3}Cu_3Ti_4O_{12}$ as mentioned above.
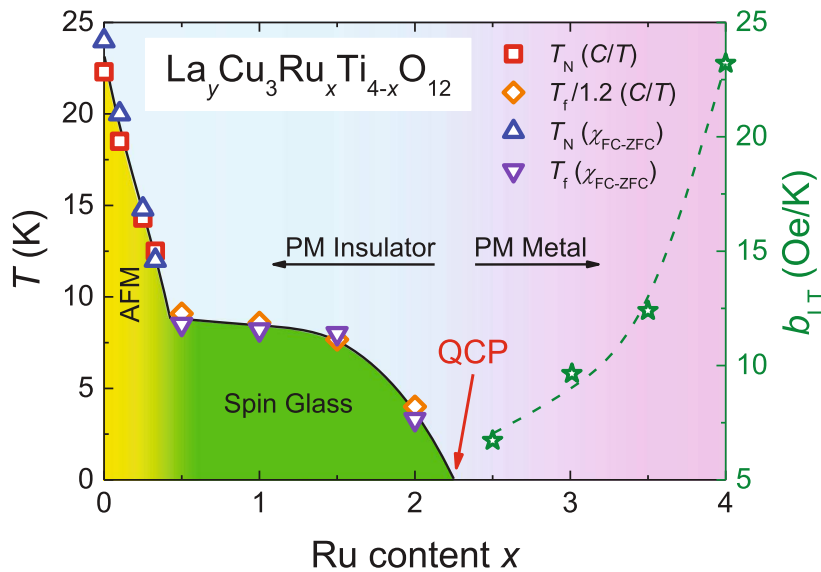
Fig. 14. Phase diagram of $La_yCu_3Ru_xTi_{4-x}O_{12}$ using characteristic transition temperatures (left scale) and low-temperature Korringa slopes (green stars) from Gd^{3+}-ESR (right scale). The Néel temperatures T_N were determined from the kink in the magnetic susceptibility (blue triangles) as well as from the maxima of the peak in the specific heat (red squares). The transition to the spin-glass state is rather smooth and, therefore, only a color change is used to indicate it. The corresponding freezing temperature T_f is obtained from the maximum in the cusp of the zfc-susceptibility (purple triangles) and the maximum of the peak in the specific heat C_p divided by 1.2 (orange rhombes). The latter value documents a reduction of the freezing temperature as typically experienced for spin-glass materials [41].

agreement with the "best fit" of the susceptibility data. The obtained behavior of the Cu and Ru local spin moments agrees well with the above described increasing delocalization of the Cu 3d electrons, which become itinerant above $x = 2.5$. On the other hand, Ru 4d electrons start to increasingly localize until $S_{Ru} \approx 0.83$ is achieved for $x = 4$, which is close to the $S = 1$ expected for the $4d^4$ low-spin configuration of Ru^{4+} ions in octahedral coordination. This fits to the strongly varying nature of the Ru d electrons reported in Ref. [71]. Furthermore, the changes in the crystal structure have to be considered. Goodenough [72] reported on an increasing localized character of electrons in octahedral BO_6 coordination when the average B–O bond length increases, which is the case for increasing x in $LaCu_3Ru_xTi_{4-x}O_{12}$. In comparison, the Cu–O bond length either slightly decreases or remains almost constant. Furthermore, the variation of the Ru–O–Ru bond angle as described in Sect. 4 has to be regarded. The slight changes of the local crystal structure and the rising number of available Ru–O–Cu exchange interaction paths per unit-cell with increasing Ru incorporation seem to support the mobility and itineracy of the Cu electrons.

9 Phase diagram

In the previous sections a considerable number of characteristic data for different phases have been obtained and discussed. Depending on the ruthenium substitution level, characteristic transition temperatures (left scale) as well as Korringa slopes (right scale) are used to construct the corresponding phase diagram shown in Fig. 14.

At $x = 0$ we start from an antiferromagnetic Mott insulator with a Néel temperature $T_N \approx 24\,\text{K}$. Here the copper spins are well localized as evident from the pure Curie-Weiss behavior of the magnetic susceptibility and the well defined Cu^{2+}-ESR signal [34]. With increasing Ru content replacing the Ti ions, T_N decreases linearly down to about $9\,\text{K}$ for $x = 0.5$, where the antiferromagnet gradually transforms into a frustrated magnet, revealing a spin-glass state. Concomitantly, the Cu-ESR signal vanishes indicating the incipient delocalization of the Cu-3d electrons [73]. On further increasing x the spin-glass state turns out to be rather stable with a freezing temperature $T_f \approx 8\,\text{K}$ until it becomes suppressed at $x \approx 2.25$, where the copper spins are supposed to become completely delocalized. Above this Ru concentration the compounds remain paramagnetic down to the lowest temperatures without any indications of AFM ordering or spin-glass transition. However, a significantly increasing conductivity, a non-zero Sommerfeld-coefficient in the specific heat C_p and most clearly a non-zero Korringa relaxation of the Gd^{3+}-ESR indicate a metallic phase for $x \geq 2.25$. Moreover, with increasing x the electronic correlations become stronger, which was observed in the magnetic susceptibility and DFT calculations, resulting in a heavy-fermion state for $LaCu_3Ru_4O_{12}$.

In total, the experimental data indicate the coincidence of the suppression of the spin-glass state around $x = 2.25$ with the occurrence of the metal-to-insulator transition in the same substitution range. This coincidence was predicted earlier from preliminary measurements and was ascribed to the existence of a quantum-critical point (QCP) in Ref. [18]. Now, the predicted value of the critical concentration $x \approx 2$ has been refined by ESR methods [21] and can be appropriately discussed in the context of the results provided in the present publication. It is not a standard scenario of a QCP albeit the suppression of a magnetic transition and the concomitant emergence of metallic conductivity represented by the Korringa slope in the phase diagram. The suppressed magnetic phase is a spin-glass state which is not a phase in terms of a thermodynamic definition. Moreover, any divergence of the effective electronic mass, usually expected at the QCP, cannot be evidenced from the behavior of the Korringa-slope or Sommerfeld coefficient, which rather are governed by a simple dilution effect.

Nevertheless, one has to take into account that the situation in $La_yCu_3Ru_x Ti_{4-x}O_{12}$ is more complicated than in a usual Mott-Hubbard scenario, because of the different magnetic systems involved. The electric conductivity emerges from the gradual delocalization of the copper 3d holes and the suppression of the corresponding spin-glass phase with increasing ruthenium content x. On the other hand, the ruthenium 4d-valence is always stable at $+4$ exhibiting a Kondo-like behavior with a characteristic temperature practically independent from x. This means that the quantum-critical behavior is to be expected rather in the copper electron system than for the ruthenium spins. Here it has to be recalled that in the related compound $CaCu_3Ru_4O_{12}$ non-Fermi liquid behavior indicating the proximity of a QCP has been observed basically in the copper subsystem at temperatures below $2\,\text{K}$ [5]. Thus, further low-temperature investigations in the milli-Kelvin regime are necessary, to better characterize the properties of the quantum-critical point in $La_yCu_3Ru_xTi_{4-x}O_{12}$.

10 Summary

We performed a comprehensive experimental investigation of the substitutional series $La_yCu_3Ru_xTi_{4-x}O_{12}$ in search for quantum criticality at the transition from an antiferromagnetic Mott insulator ($x = 0$) with colossal dielectric constants to a d-electron derived heavy-fermion metal ($x = 4$). The structural and physical

properties were characterized on polycrystalline materials prepared by solid-state reaction. X-ray diffraction confirmed the phase purity of all samples which all crystallize in the same cubic space group $Im\bar{3}$. Only the cell parameter a increases monotonously with increasing substitution levels x and y.

From the inverse magnetic susceptibility effective magnetic moments and Curie-Weiss (CW) temperatures were obtained by means of pure Curie-Weiss fits in the temperature range above 300 K. Here the effective magnetic moments μ_{eff} are in good agreement with the theoretical estimates of Ru^{4+} plus Cu^{2+} moments. The CW temperatures Θ_{CW} change from -100 K down to -1000 K in the range $1 \leq x \leq 3$ indicating the strong increase of the exchange with increasing influence of the Ru $4d$ orbitals. For expanding the CW-fits to the range $100 \leq T \leq 400$ K an additional temperature-independent term χ_0 was introduced to describe Pauli-paramagnetic as well as van-Vleck contributions and to account for the non-linearity of $1/\chi$ in this temperature regime. From these fits a minimum of μ_{eff} was obtained for $x \approx 2$ and the CW temperature decreases gradually to -700 K for increasing Ru concentration. From this behavior it can be concluded that the high temperature fit shows the expected spin-only magnetism for $La_yCu_3Ru_xTi_{4-x}O_{12}$, while at low temperatures the delocalization of the Cu electrons predicted by band-structure calculations and the Kondo-screening effect at the Ru ions play major roles. The existence of a spin-glass state was endorsed for the substitution range $0.5 \leq x \leq 2.25$ using field-cooled and zero-field-cooled as well as AC-susceptibility measurements.

The antiferromagnetic order observed for low Ru contents ($x \leq 0.5$) as well as the transition to the spin-glass state ($x \leq 2.25$) can be clearly observed in the specific-heat data. The area below the transition peak was determined after subtraction of the phonon contributions to the specific heat. From this area the magnetic entropy S_Δ of the transition was obtained and, hence, the effective spin-moment per copper ion S was calculated using $S_\Delta = 3 \cdot R \ln (2S + 1)$. For $x = 0$ a good agreement was found with $S = 1/2$, however for increasing Ru content the effective moment decreases monotonously and vanishes almost for $x \geq 2$, which can be explained by increasing delocalization of the Cu electrons according to the evaluation of χ at intermediate temperatures. Furthermore, it was found that the electronic contribution to the specific heat (Sommerfeld coefficient) strongly increases for $x \geq 2.5$, which correlates with the increasing Kondo-like behavior of heavy-fermion systems in the Ru-rich phase. At the same time the electrical resistivity in this Ru-rich phase $x \geq 2$ reflects the transition from a semiconducting to a metallic phase close to $x = 2.25$ with the Kondo-like behavior.

The longitudinal spin-relaxation rate $1/T_1$ obtained in nuclear quadrupole resonance (NQR) measurements of ^{63}Cu in $LaCu_3Ru_4O_{12}$ reveals a purely linear Korringa law with a slope comparable to that in copper metal. In contrast, the ESR linewidth observed for Gd-doped $La_yCu_3Ru_xTi_{4-x}O_{12}$ with high ruthenium contents exhibits an enhanced slope below $T_{\text{coh}} \approx 50$ K and flattens at higher T. As the Korringa-slope is directly connected to the density-of-states at the Fermi-level in metallic systems these results indicate locally different density-of-states at Cu- and Gd-site: While the Cu-site is not affected by the heavy-fermion formation, Gd detects the spin fluctuation at the Ru-site. This is in agreement with NQR experiments in $CaCu_3Ru_4O_{12}$, where the Korringa rate is strongly enhanced in comparison with Ru-metal in ^{101}Ru NQR but slightly lower than in Cu-metal in ^{63}Cu NQR [18]. The increased slope when compared with canonical metals once more supports the heavy-fermion behavior.

The experiments have been accompanied by systematic DFT band-structure calculations utilizing local spin-density-approximation LSDA. In the density-of-states Cu and Ru bands with d-orbital character are located at the Fermi-energy. The contributions of the Ti $3d$ orbitals are found in the range 1 eV to 3 eV above E_F. The Cu $3d$ bands are gradually shifted to lower energies by approximately 1 eV with

increasing Ru content indicating a decrease of the copper valence. Furthermore, a stronger hybridization with the ruthenium bands is visible. Thus, a decreasing local Cu spin moment is obtained with increasing x in agreement with the findings in the specific-heat and magnetic-susceptibility data. On the other hand, the Ru $4d$ spin moments are increasingly localized for higher Ru concentrations $x > 2$ according to a local heavy-fermion formation at the Ru-site.

Both, experimental data and DFT calculations indicate the increasing delocalization of the copper electrons with increasing x, finally resulting in a metallic state for $x \geq 2.25$. Although the electronic mass enhancement is clearly connected to the Kondo-like behavior of the ruthenium spins and their concentration x, the copper system seems to cross a quantum-critical point at $x \approx 2.25$ starting from an antiferromagnetic ground state of localized spins ($x = 0$) via a spin-glass phase ($0.5 \leq x \leq 2.25$) into complete delocalization for $x \geq 2.25$. The detailed properties of this QCP should be elucidated by further detailed experiments in the milli-Kelvin regime.

References

1. C.C. Homes, T. Vogt, S.M. Shapiro, S. Wakimoto, A.P. Ramirez, Science **293**, 673 (2001)
2. P. Lunkenheimer, R. Fichtl, S.G. Ebbinghaus, A. Loidl, Phys. Rev. B **70**, 172102 (2004)
3. Z. Zeng, M. Greenblatt, M.A. Subramanian, M. Croft, Phys. Rev. Lett. **82**, 3164 (1999)
4. W. Kobayashi, I. Terasaki, J. Takeya, I. Tsukada, Y. Ando, J. Phys. Soc. Jpn. **73**, 2373 (2004)
5. A. Krimmel, A. Günther, W. Kraetschmer, H. Dekinger, N. Büttgen, A. Loidl, Phys. Rev. B **78**, 165126 (2008)
6. S. Tanaka, N. Shimazui, H. Takatsu, S. Yonezawa, Y. Maeno, J. Phys. Soc. Jpn. **78**, 024706 (2009)
7. S. Kondo, D.C. Johnston, C.A. Swenson, F. Borsa, A.V. Mahajan, L.L. Miller, T. Gu, A.I. Goldman, M.B. Maple, D.A. Gajewski, E.J. Freeman, N.R. Dilley, R.P. Dickey, J. Merrin, K. Kojima, G.M. Luke, Y.J. Uemura, O. Chmaissem, J.D. Jorgensen, Phys. Rev. Lett. **78**, 3729 (1997)
8. A. Krimmel, A. Loidl, M. Klemm, S. Horn, H. Schober, Phys. Rev. Lett. **82**, 2919 (1999)
9. A. Krimmel, A. Günther, W. Kraetschmer, H. Dekinger, N. Büttgen, V. Eyert, A. Loidl, D.V. Sheptyakov, E.-W. Scheidt, W. Scherer, Phys. Rev. B **80**, 121101 (2009)
10. A.P. Ramirez, G. Lawes, D. Li, M.A. Subramanian, Solid State Commun. **131**, 251 (2004)
11. I. Tsukuda, R. Kammuri, T. Kida, S. Yoshii, T. Takeuchi, M. Hagiwara, M. Iwakawa, W. Kobayashi, I. Terasaki, Phys. Rev. B **79**, 054403 (2009)
12. S.G. Ebbinghaus, A. Weidenkaff, R.J. Cava, J. Solid State Chem. **167**, 126 (2002)
13. M. Labeau, B. Bochu, J.C. Joubert, J. Chenavas, J. Solid State Chem. **33**, 257 (1980)
14. T. Sudayama, Y. Wakisaka, K. Takubo, T. Mikozawa, W. Kobayashi, I. Terasaki, S. Tanaka, Y. Maeno, M. Arita, H. Namatame, M. Taniguchi, Phys. Rev. B **80**, 075113 (2009)
15. S.G. Ebbinghaus, S. Riegg, T. Götzfried, A. Reller, Eur. Phys. J. Special Topics **180**, 91 (2010)
16. A. Günther, Ph.D. thesis, Augsburg, 2015

17. B. Bochu, M.N. Deschizeaux, J.C. Joubert, A. Collomb, J. Chenavas, M. Marezio, J. Solid State Chem. **29**, 291 (1979)
18. N. Büttgen, H.-A. Krug von Nidda, W. Krätschmer, A. Günther, S. Widmann, S. Riegg, A. Krimmel, A. Loidl, J. Low Temp. Phys. **161**, 148 (2010)
19. S. Riegg, A. Reller, A. Loidl, S.G. Ebbinghaus, Dalton Trans. **44**, 10852 (2015)
20. B. Bochu, J. Chenavas, J.C. Joubert, M. Marezio, J. Solid State Chem. **11**, 88 (1974)
21. B. Schmidt, H.-A. Krug von Nidda, S. Riegg, S.G. Ebbinghaus, A. Reller, A. Loidl, Magn. Resonance Solids **16**, 14210 (2014)
22. J. Rodriguez-Carvajal, Physica B **192**, 55 (1993)
23. K. Koepernick, H. Eschrig, Phys. Rev. B **59**, 1743 (1999)
24. I. Opahle, K. Koepernick, H. Eschrig, Phys. Rev. B **60**, 14035 (1999)
25. A.M. Glazer, Acta Crystallogr. Sect. B **28**, 3384 (1972)
26. P.M. Woodward, Acta Crystallogr. Sect. B **53**, 32 (1997)
27. A.N. Vasil'ev, O.S. Volkova, Low Temp. Phys. **33**, 895 (2007)
28. T. Hahn, *International Tables for Crystallography, Volume A, Space-Group Symmetry*, 5th edition (John Wiley & Sons, New York, 2005)
29. A. Deschanvres, B. Raveau, F. Tollemer, Bull. Soc. Chim. Fr. **11**, 4077 (1967)
30. M.A. Subramanian, D. Li, N. Duan, B.A. Reisner, A.W. Sleight, J. Solid State Chem. **151**, 323 (2000)
31. M.A. Subramanian, A.W. Sleight, Solid State Sci. **4**, 347 (2002)
32. R.D. Shannon, Acta Crystallogr. Sect. A **32**, 751 (1976)
33. J. Muller, A. Haouzi, C. Laviron, M. Labeau, J.C. Joubert, Mater. Res. Bull. **21**, 1131 (1986)
34. A. Dittl, S. Krohns, J. Sebald, F. Schrettle, M Hemmida, H.-A. Krug von Nidda, S. Riegg, A. Reller, S.G. Ebbinghaus, A. Loidl, Eur. Phys. J. B **79**, 391 (2011)
35. W.H. Brumage, C.R. Yarger, C.C. Lin, Phys. Rev. **133**, A765 (1964)
36. M.M. Kreitman, F.J. Milford, R.P. Kenan, J.G. Daunt, Phys. Rev. **144**, 367 (1966)
37. F.J. Brieler, P. Grundmann, M. Fröba, L.M. Chen, P.J. Klar, W. Heimbrodt, H.-A. Krug von Nidda, T. Kurz, A. Loidl, Chem. Mater. **17**, 795 (2005)
38. F.J. Brieler, P. Grundmann, M. Fröba, L.M. Chen, P.J. Klar, W. Heimbrodt, H.-A. Krug von Nidda, T. Kurz, A. Loidl, Eur. J. Inorg. Chem. **18**, 3597 (2005)
39. M.B. Maple, R.P. Dickey, J. Herrmann, M.C. de Andrade, E.J. Freeman, D.A. Gajewski, R. Chau, J. Phys.: Condens. Matter **8**, 9773 (1996)
40. Y.J. Kim, S. Wakimoto, S.M. Shapiro, P.M. Gehring, A.P. Ramirez, Solid State Commun. **121**, 625 (2002)
41. J.A. Mydosh, *Spin Glasses: An Experimental Introduction* (Taylor & Francis, London, 1993)
42. K. Binder, A.P. Young, Rev. Mod. Phys. **58**, 801 (1986)
43. M. Ocko, D. Drobac, B. Buschinger, C. Geibel, F. Steglich, Phys. Rev. B **64**, 195106 (2001)
44. N. Büttgen, R. Böhmer, A. Krimmel, A. Loidl, Phys. Rev. B **53**, 5557 (1996)
45. R. Spitzfaden, A. Loidl, J.-G. Park, B.R. Coles, J. Phys.: Condens. Matter **8**, 2857 (1996)
46. H.-A. Krug von Nidda, A. Schütz, M. Heil, B. Elschner, A. Loidl, Phys. Rev. B **57**, 14344 (1998)
47. S. Mair, H.-A. Krug von Nidda, M. Lohmann, A. Loidl, Phys. Rev. B **60**, 16409 (1999)
48. B. Elschner, A. Loidl, in *Handbook on the Physics and Chemistry of Rare Earths*, Vol. 24, edited by K.A. Gschneidner Jr., L. Eyring (Elsevier Science B.V., Amsterdam, 1997), p. 221
49. S.E. Barnes, Adv. Phys. **30**, 801 (1981)
50. M. Hanabusa, T. Kushida, Phys. Rev. B **5**, 3751 (1972)
51. M. Schlott, B. Elschner, M. Herrmann, W. Assmus, Z. Phys. B **72**, 385 (1988)
52. H.R. Ott, Z. Fisk, *Handbook on the Physics and Chemistry of the Actinides*, edited by A.J. Freeman, G.H. Lander (Elsevier, Amsterdam, 1987)

53. N. Grewe, F. Steglich, *Handbook on the Physics and the Chemistry of the rare earths*, Vol. 14, edited by K.A. Gschneidner Jr., L. Eyring (Elsevier, Amsterdam, 1991)
54. M. Coldea, H. Schaeffer, V. Weissenberger, B. Elschner, Z. Phys. B **68**, 25 (1987)
55. M. Heinrich, H.-A. Krug von Nidda, V. Fritsch, A. Loidl, Phys. Rev. B **63**, 193103 (2001)
56. H.-A. Krug von Nidda, R. Bulla, N. Büttgen, M. Heinrich, A. Loidl, EPJ B **34**, 399 (2003)
57. Y. Tokura, Y. Taguchi, Y. Okada, Y. Fujishima, T. Arima, K. Kumagai, Y. Iye, Phys. Rev. Lett. **70**, 2126 (1993)
58. Y. Taguchi, Y. Tokura, T. Arima, F. Inaba, Phys. Rev. B **48**, 511 (1993)
59. L. He, J.B. Neaton, M.H. Cohen, D. Vanderbilt, C.C. Homes, Phys. Rev. B **65**, 214112 (2002)
60. L. He, J.B. Neaton, D. Vanderbilt, M.H. Cohen, Phys. Rev. B **67**, 012103 (2003)
61. S.B. Fagan, A.G. Souza Filho, A.P. Ayala, J. Mendes Filho, Phys. Rev. B **72**, 014106 (2005)
62. G.-L. Li, Z. Yin, M.-S. Zhang, Phys. Lett. A **344**, 238 (2005)
63. H. Shiraki, T. Saito, T. Yamada, M. Tsujimoto, M. Azuma, H. Kurata, S. Isoda, M. Takano, Y. Shimakawa, Phys. Rev. B **76**, 140403 (2007)(R)
64. M. Matos, L. Walmsley, J. Phys.: Condens. Matter **18**, 1793 (2006)
65. J.-C. Zheng, A.I. Frenkel, L. Wu, J. Hanson, W. Ku, E.S. Božin, S.J.L. Billinge, Y. Zhu, Phys. Rev. B **81**, 144203 (2010)
66. J.H. Clark, M.S. Dyer, R.G. Palgrave, C.P. Ireland, J.R. Darwent, J.B. Claridge, M.J. Rosseinsky, J. Am. Chem. Soc. **133**, 1016 (2011)
67. U. Schwingenschlögl, V. Eyert, U. Eckern, Chem. Phys. Lett. **370**, 719 (2003)
68. S.F. Matar, M.A. Subramanian, Mater. Lett. **58**, 746 (2004)
69. K. Koepernick, B. Velicky, R. Hayn, H. Eschrig, Phys. Rev. B **55**, 5717 (1997)
70. Ch. Kant, T. Rudolf, F. Mayr, S. Krohns, P. Lunkenheimer, S.G. Ebbinghaus, A. Loidl, Phys. Rev. B **77**, 045131 (2008)
71. R.J. Cava, Dalton Transact. **2004**, 2979 (2004)
72. J.B. Goodenough (eds.), *Structure and Bonding, Localized to Itinerant Electronic Transition in Perovskite Oxides, General Considerations* (Springer, Berlin–Heidelberg 2001), p. 1
73. A. Dittl (private communication)